Citation for published version:
Hualca Tigsilema, FP, Horwood, J, Sangan, C, Lock, G & Scobie, J 2019, 'The Effect of Vanes and Blades on Ingress in Gas Turbines', *Journal of Engineering for Gas Turbines and Power: Transactions of the ASME*. https://doi.org/10.1115/1.4045149

DOI:
10.1115/1.4045149

Publication date:
2019

Document Version
Peer reviewed version

Link to publication

Publisher Rights
CC BY
(C) ASME 2019.

University of Bath

General rights
Copyright and moral rights for the publications made accessible in the public portal are retained by the authors and/or other copyright owners and it is a condition of accessing publications that users recognise and abide by the legal requirements associated with these rights.

Take down policy
If you believe that this document breaches copyright please contact us providing details, and we will remove access to the work immediately and investigate your claim.

Download date: 23. Jan. 2020

The Effect of Vanes and Blades on Ingress in Gas Turbines

Fabian P Hualca, Joshua TM Horwood, Carl M Sangan, Gary D Lock and James A Scobie
f.hualca@bath.ac.uk, j.t.m.horwood@bath.ac.uk, c.m.sangan@bath.ac.uk, g.d.lock@bath.ac.uk and j.a.scobie@bath.ac.uk
Department of Mechanical Engineering
University of Bath
Bath, BA2 7AY
United Kingdom

ABSTRACT

This paper presents experimental and computational results using a 1.5-stage test rig designed to investigate the effects of ingress through a double radial overlap rim-seal. The effect of the vanes and blades on ingress was investigated by a series of carefully-controlled experiments: firstly, the position of the vane relative to the rim seal was varied; secondly, the effect of the rotor blades was isolated using a disc with and without blades.

Measurements of steady pressure in the annulus show a strong influence of the vane position. The relationship between sealing effectiveness and purge flow-rate exhibited a pronounced inflexion for intermediate levels of purge; the inflexion did not occur for experiments with a bladeless rotor. Shifting the vane closer to the rim-seal, and therefore the blade, caused a local increase in ingress in the inflexion region; again this effect was not observed for the bladeless experiments.

Unsteady pressure measurements at the periphery of the wheel-space revealed the existence of large-scale pressure structures (or instabilities) which depended weakly on the vane position and sealing flow rate. These were measured with and without the blades on the rotor disc. In all cases these structures rotated close to the disc speed.

1 INTRODUCTION

The efficiency of a gas turbine can be increased by raising the Turbine Entry Temperature (TET). In modern engines the TET exceeds the melting point of the materials used in the manufacture of the vanes, blades and discs. Integrity and reliability of these components is controlled by employing cooling systems to maintain metal temperatures at an acceptable level; approximately 20-25% of the mainstream flow is bled off from the compressor and used for cooling purposes. The distribution of cooling air is handled by the secondary-air system, which directs flow to the vanes, blades and cavities formed between the rotating and stationary discs.

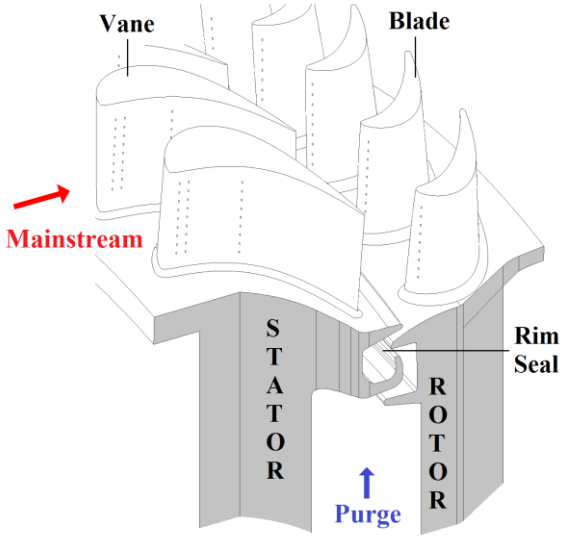

Figure 1: A generic high-pressure gas turbine stage with a rim-seal fitted at the periphery of the cavity

Ingress of hot mainstream flow into the discs cavities has a detrimental effect on the operating life of the turbine. Sealing air is used, in combination with a rim-seal at the periphery of the cavity, to suppress, or in the limit prevent, ingress; sealing air is also used to dissipate the heat generated by windage. A typical sealing arrangement for a high-pressure turbine stage is shown in Figure 1. A sensitive balance exists, where sufficient cooling air must be supplied to protect the highly-stressed components, whilst

similarly avoiding an unnecessary penalty on cycle efficiency created by the superfluous use of bleed air.

The complex interaction between vanes and blades in the turbine annulus creates a pressure variation in the proximity of the rim-seal that is unsteady and difficult to predict; the pressure across the rim-seal is directly related to the ingress into the cavity. Furthermore, the individual contribution from the vanes and blades with respect to the local pressure driving the ingestion is unknown. Conclusions from the literature in this regard are often contradictory and unestablished.

This paper presents experimental and computational results from a 1.5-stage gas turbine test rig, designed to investigate hot gas ingestion into the cavities formed upstream and downstream of the rotor disc; a double radial-clearance rim-seal was installed in the upstream cavity. The axial distance between the vane trailing-edge and the rim-seal was varied in order to interrogate the effect of the vane pressure field on the performance of the rim-seal. The effect of the blade on ingestion was examined by conducting tests with both a *bladed* and *bladeless* rotor.

Section 2 reviews literature relevant to the topic of hot gas ingestion in turbines, with a focus on studies concerned with the effect of vanes and blades on the performance of rim-seals. Section 3 introduces the experimental facility and operating conditions. Section 4 details the computational model used to predict pressure variations in the annulus. Experimental data and comparisons with the computational model are presented in Section 5. Conclusions are presented in Section 6.

2 LITERATURE REVIEW

This section reviews publications related to the influence of vanes and blades on ingress. For a more extensive review of the topic in general, the reader is referred to recent reviews by Scobie *et al.* [1] and Chew *et al.* [2].

Green and Turner [3] conducted the first experimental study examining the combined effect of stator vanes and rotor blades on ingress; the rim seal clearance was positioned close to the blade leading edge. Surprisingly it was found that the measured ingress with both vanes and blades was less than the ingress with the blades removed.

Chew *et al.* [4] described a combined experimental and computational study including stator vanes at three axial positions in the absence of blades. They showed that for the majority of the experimental range the asymmetry in the annulus flow was the dominant driver for ingress. Ingress was shown to reduce as the vanes were moved further upstream away from the rim seal.

Hills *et al.* [5] described a combined experimental and computational study including vanes and blades modelled as rotor 'pegs'. 3D steady CFD was used to predict the circumferential pressure variations produced by the vanes in the annulus upstream of the rim seal. Good agreement was demonstrated at lower sealing flow rates however at higher flow rates the experimental and computational results diverged due to the complex interaction of the sealing and mainstream flows. The authors concluded that predicting ingress is considerably more difficult than predicting annulus pressure variations, and that a combined CFD model featuring annulus and wheel-space flows is required to completely capture the interaction.

Hills *et al.* [6] used unsteady CFD to show better agreement with the experimental data than previous steady computations. A significant influence on ingress was caused by the circumferential pressure distribution from the rotating 'pegs,' even though these asymmetries were of lesser magnitude than those created by the stationary vanes. They

concluded that the vane-only measurements made by Green and Turner [3] were in error, and that blades do in fact contribute to ingress. Differences in ingress between experiments and computations were associated with discrepancies between measured and calculated pressure asymmetries in the annulus.

Bohn *et al.* [7] studied ingress in a single-stage rig at Aachen without blades but with 30 vanes upstream of the rim seal. The axial decay of the peak-to-trough pressure variation was measured at different positions downstream of the vane trailing edge on the hub platform in the annulus. Levels of ingress increased as the rim seal encountered larger pressure asymmetries with the vane closest to the rim seal.

Later Bohn *et al.* [8] incorporated a set of 62 rotor blades and used measurements of gas concentration to assess the effects of Re_w and Re_ϕ on the effectiveness for two simple rim seals. Increasing Re_w increased the annulus circumferential pressure asymmetry with increased ingress for both seals. A steady 3D CFD sector model (no blades) identified large-scale structures near the rotating disc; these low-pressure lobes varied in diameter with circumferential position.

Bohn *et al.* [9] compared their experimental findings with and without rotor blades. The blades were shown to have a surprisingly large effect on the pressure asymmetry measured on the platform downstream from the vane trailing edge. The blades adversely affected the sealing performance of a simple axial gap with flat rotor and stator discs. However for a second seal geometry consisting of an axial lip on the stator disc, the blades were shown to have a favourable effect. 3D unsteady CFD calculations of the second geometry confirmed the favourable influence of the blades on sealing effectiveness.

Bohn *et al.* [10] made LDV measurements on a different configuration of the rig featuring 16 vanes upstream and downstream of 32 blades. Both the vanes and blades

strongly influenced ingress into the upstream cavity, even at significant purge. Ingress was measured to intensify when the blades interacted with the stator wake.

Jakoby *et al.* [11] conducted a numerical study on the unsteady pressure field in the Aachen rig. Multiple models were considered, however only a 360° URANS model without blades or vanes was able to capture large-scale structures rotating in the wheel-space at 0.8 of the disc speed. The structures were shown to increase ingress at low purge, but were supressed at higher sealing flows.

Wang *et al.* [12] used 3D unsteady CFD to investigate the effect of axial spacing between the vanes and blades, and the axial location of the rim seal. Time-average ingestion characteristics for wide and close spaced stage configurations were shown to be approximately the same when the seal was located the same distance upstream of the blade leading edge. The blade pressure field was shown to be the dominant cause of ingestion for all three configurations considered.

Rabs *et al.* [13] showed computationally that the large scale structures could exist without vanes or blades. They attributed the effect to Kelvin-Helmholtz instabilities, and went on to show the addition of the blades acts to suppress the spectral activity.

Beard *et al.* [14] showed similar unsteady behaviour in the absence of both blades and vanes. They observed low-pressure structures with $f / f_d \approx 22$ across all sealing flow rates tested. The number of instabilities near the rim-seal reduced from $N = 28/29$ to 26/27 as the sealing flow increased. These structures were measured to rotate at 0.8 of the disc speed across all the conditions tested.

Savov *et al.* [15] experimentally studied two different rim seal configurations, with and without blades for a wide range of conditions. They identified frequencies $f / f_d \approx$ 20-40 attributed to unstable shear layers in the rim seal, previously discussed by Rabs *et al.* [13]. Blades were shown to supresses the intensity of the unsteadiness.

3 EXPERIMENTAL FACILITY

This section describes the measurement capability of the University of Bath research facility – see Patinios *et al.* [16]. The rig creates an engine-scaled environment at a tenth of the Reynolds number found in typical turbines, and models ingress into wheel-spaces upstream and downstream of a rotor. The operating conditions at low-temperature and low-pressure offer a benign environment for instrumentation access, efficiency, flexibility and relatively low cost.

3.1 Test rig

Compressed air was supplied through a transition inlet to an annulus, creating an axisymmetric mainstream flow through the 1.5-stage axial turbine stage. The rotor (manufactured as a titanium *blisc*) consisted of 48 turned blades. The upstream and downstream stators (manufactured as bladed rings) each had 32 vanes. The disc diameter was 380 mm and the annulus height was 25 mm. The rotor disc was connected to a shaft by a hydraulic coupling. The design rotational speeds are 3000 and 4000 rpm with power absorbed by a dynamometer rated at 34 kW.

Purge was introduced to the upstream wheel-space at low radius through an inlet seal, with flow rates measured and carefully controlled by valves and thermal mass-flow meters; sealing mass-flow-rate was metered to an accuracy of ± 1% of the full-scale range. Pressure was measured using multi-channel scani-valves, instrumented with differential transducers with an accuracy of ± 0.3% of the measurement range.

The sealing flow parameter is defined as

$$\Phi_0 = \frac{C_{w,0}}{2\pi G_c \mathrm{Re}_\phi} = \frac{U}{\Omega b} \tag{3.1}$$

with all symbols defined in the nomenclature.

3.2 Operating conditions

Experimental measurements were conducted at two operating conditions; Table 1 shows the important test parameters. The flow immediately downstream of the vanes was at near atmospheric pressure; although the Mach number was low (M < 0.45), compressibility effects were considered in determining the governing non-dimensional parameters. The static temperature and pressure measured inside the upstream wheel-space (at r/b = 0.958) was used to determine the speed of sound, air density and viscosity.

Parameters	**Disc Speed (RPM)**	
	3000	**4000**
Rotational Reynolds Number, $\mathbf{Re}_\phi$	7.4×10^5	1.0×10^6
Axial Reynolds Number, $\mathbf{Re}_w$	3.0×10^5	4.1×10^5
Flow Coefficient, C_F	0.407	0.407
Vane exit Mach Number, M	0.33	0.44

Table 1: Test rig operating conditions

3.3 Vane details

The modular design of the test rig allowed two vane configurations to be tested expediently and efficiently. The original vane configuration, referred to below as vane-P1, was used previously by Patinios *et al.* [16] and Horwood *et al.* [17]. The axial distance between the upstream edge of the rim-seal gap and vane trailing-edge was 5

mm. The second vane set, vane-P2, is geometrically identical in terms of profile, however the axial location was displaced 2.5 mm closer towards the edge of the seal.

3.4 Double radial-clearance rim seal

In this paper a generic double radial-clearance rim seal with no commercial proprietary (*i.e.* intellectual property) was used in the upstream wheel-space. Figure 2 shows the geometric configuration of the seal with important dimensions listed in Table 2. Vanes P1 and P2 are identical in profile and axial chord. The two axial vane positions are highlighted in red and blue.

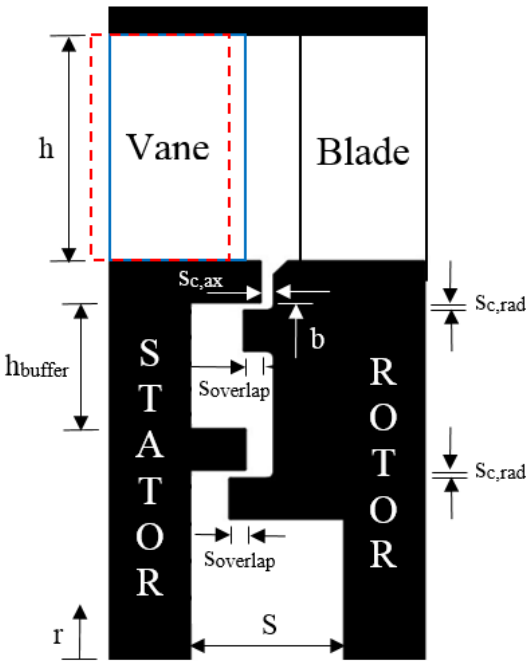

Figure 2: Double radial-clearance seal configuration in the upstream wheel-space

Parameter	Dimension (mm)
h	25
b	190
S	20
h_{buffer}	16.5
$s_{c,ax}$	2
$s_{overlap}$	1.86
$s_{c,rad}$	1.28

Table 2: Double radial-clearance rim seal parameters

3.5 Pressure measurements in the annulus

The variation of *steady* pressure over the vane pitch was measured at five different locations in the rig. The A locations are on the hub platform of the stator disk, and the B locations are on the shroud of the annulus in the outer casing. The pressure instrumentation consisted of 15 pressure taps (diameter 0.5mm), spanning a vane pitch of 11.25° ($0 < \theta < 1$). Typical measurement locations are shown on the stator hub of annulus in Figure 3.

3.6 Wheel-space measurements

Figure 3 illustrates a cutaway view of the rig test section. CO_2 is used as a tracer gas for measurements of concentration in the wheel-space. Pressure and concentration were measured at radial locations on the stator disc and (using hypodermic tubes) in the rotating core between stator and rotor. Although not presented in this paper,

concentration effectiveness has been shown to be circumferentially independent over one vane pitch in the wheel-space [16].

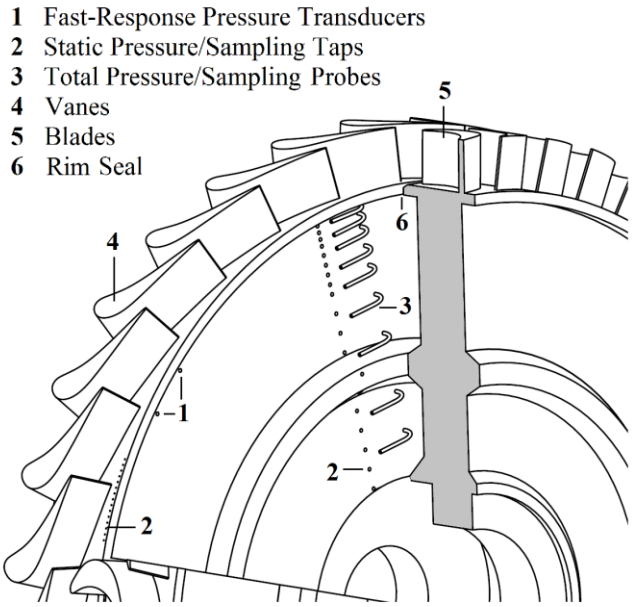

Figure 3: Test section and instrumentation

The tracer gas was extracted to an analyser (Signal-Group 9000MGA); the repeatability and a linearity of gas analysis was greater than ±1% and 0.5% of the full-scale range respectively [16].

The effectiveness based on concentration measurements (c) is defined as

$$\varepsilon_c = \left(\frac{c - c_a}{c_0 - c_a}\right) \qquad (3.2)$$

where the subscripts a and 0 respectively denote the annulus and purge inlet to the wheel-space. The local concentration (c) is measured using taps on the stator or through hypodermic tubes in the core of the wheel-space. From Equation (3.2), ε_c is unity when the wheel-space is fully purged and ε_c is zero when there is no sealing flow. The purge seed level was 0.5 - 1% CO_2; the inherent concentration of the annulus flow was c_a ~ 0.04%.

Total and static pressure measured in the wheel-space were used to calculate the tangential component of velocity in the core from Bernoulli's equation:

$$V_\phi = \left[\frac{2(p_T - p)}{\rho}\right]^{1/2} \tag{3.3}$$

The swirl ratio of the fluid in the inviscid core between the boundary layers in the wheel-space is defined as

$$\beta = \frac{V_\phi}{\Omega \mathrm{r}} \tag{3.4}$$

3.7 Unsteady pressure measurements in the wheel-space

Experiments of unsteady pressure were conducted in the wheel-space. Measurements were taken at two locations using Kulite XCS-062-1PSI transducers. The Kulite ultra-miniature sensors have a diameter of 1.7 mm and a length of 3 mm, with a characteristic natural frequency of 150 kHz and are temperature compensated from 10°C to 30°C. At 4000 rpm the blade-passing-frequency, BPF = 3.2 kHz, which is significantly lower than the manufacturer quoted natural frequency. The sensors were flush mounted to the cover plate of the stator disk and were positioned strategically just below the vane platform lip, to detect the unsteadiness near seal region.

The sensors were circumferentially-spaced at the same PCD. The angle between the sensors was α = 8° at a radial position *r/b* = 0.993. Unsteady pressure data at $\mathrm{Re}_\phi = 7.4\times10^5$ is presented and discussed in Section 5.4. Although not presented in this paper, Horwood *et al.* [17] has shown the results to be Re_ϕ independent. The unsteady data was sampled at 100 kHz for 10 seconds, equivalent to 500 disk revolutions. The results were computed using a Fast Fourier Transform (FFT) of windowed segments of the signals. A rectangular window was used to obtain frequency resolution and reduced

spectral leakage. The measurements are presented non-dimensionally in the form of a pressure coefficient $C_{p.}$

4 COMPUTATIONAL MODEL

Computing the complex, unsteady flow field governing ingress has proved difficult for numerous authors; whilst some have managed to capture flow features qualitatively (Schadler *et al*. [18], Horwood *et al*. [17]), thus far no studies have demonstrated a reliable prediction of ingress levels. Accurately capturing the main gas path using CFD is more straightforward, therefore, computationally, this study focussed on the influence of vanes and blades over the annulus pressure distribution.

The Deutsches Zentrum für Luft- und Raumfahrt (DLR) solver TRACE v9.0 was employed to compute Unsteady Reynolds-Averaged Navier-Stokes (URANS) solutions using a finite-volume approach. The computational setup was largely the same as that presented by Horwood *et al*. [17], with the computed domain including the wheel-space alongside 2 vanes and 3 blades (bladed configuration only) in a 22.5º sector. Structured meshes were generated using NUMECA AutoGrid5 with y+ ~ 1 on the annulus hub and wheel-space surfaces and a y+ ~ 25 on vane, blade and shroud surfaces. The rotating and stationary domains of the bladed grids were separated by a non-matching interface ~ 1 mm upstream of the seal, while the bladeless grids were in an entirely stationary domain. The four meshes contain $4.5 \times 10^6 – 5.2 \times 10^6$ cells.

Second order Euler-backward and Fromm schemes were used for temporal and spatial discretization, while the shear stress transport model was chosen for turbulence closure. A dual time-stepping approach used 3840 time-steps per disc revolution, alongside 20 sub-iterations per time-step and a Courant-Friedrich-Levy number of 100. Sensitivity studies reported by Horwood *et al*. [17] indicated an invariance to both

increased mesh and timestep resolution. The inlet boundary conditions specified the turbulence intensity and length scale, the total temperature and the flow angles. The total pressure at the stage inlet, static pressure at stage outlet, and purge mass-flow at inlet to the wheel-space were also specified.

Computations were performed only at the higher experimental Reynolds number ($Re_\phi \sim 1.0 \times 10^6$) to restrict cost. Unsteady computations were initialised from steady mixing-plane solutions. All solutions achieved average residual levels $< 10^{-6}$ and maximum residual levels $< 10^{-3}$, alongside unchanging behaviour in flow variables.

5 RESULTS

This section presents distributions of pressure, swirl ratio and concentration effectiveness in the annulus and wheel-space over a range of purge flow rates. Section 5.1 compares steady measurements of static pressure in the annulus with time-averaged computations in both the stationary and rotating domains. Section 5.2 discusses the experimentally measured variation of swirl ratio in both the inner and outer wheel-spaces. Gas concentration measurements are used in Section 5.3 to determine the amount of ingress into the wheel-space from the annulus. Section 5.4 presents unsteady pressure measurements at the periphery of the wheel-space near the rim seal.

5.1 Annulus pressure distribution

The circumferential variation of time-averaged static pressure at the hub of the annulus is shown in Figure 4. Data is collected 1.5 mm upstream of the rim seal leading edge for the two vane positions, colour-coded with reference to the silhouette. The experimental results are plotted over two vane pitches separated by 180° in the annulus:

$0 < \theta < 1$ at (arbitrarily) 0° and $1 < \theta < 2$ at 180°. The non-dimensional pressure ($C_{p,a}$) is defined in the nomenclature.

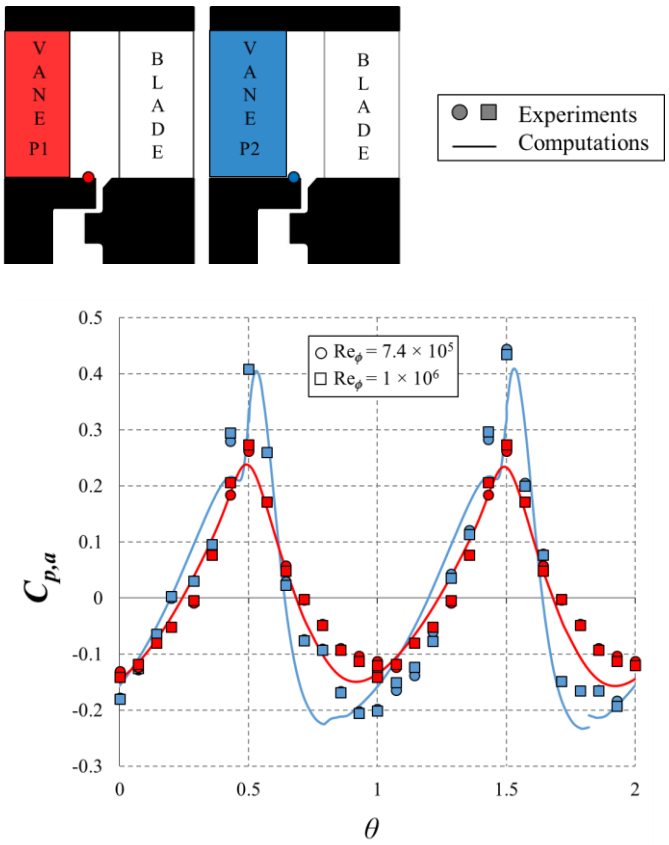

Figure 4: Circumferential distribution of steady pressure coefficient in the annulus over two non-dimensional vane pitches (Φ_0 = 0.03). Data is colour-coded with the silhouette.

The experimental results show the peak-to-trough pressure difference ($\Delta C_{p,a}$) is larger when the vane trailing edge is closer to the rim seal and measurement location. Also, the non-dimensional pressure distributions are seen to be virtually independent of Re_ϕ. There is good agreement between experimental and computational results. This comparison was taken at Φ_0 = 0.03; similarly good agreement was found at other levels

of purge. Note there is a second-order effect of Φ_0 on distributions of $C_{p,a}$ at the hub often referred to as the *spoiling effect* that is not presented here [19].

Figure 5 shows the variation of $\Delta C_{p,a}$ (see nomenclature) along the annulus hub for the two vane positions. The data presented is taken at $\Phi_0 = 0.03$. The horizontal axis (x) is geometrically aligned with the silhouette of the rim seal, with $x = 0$ at the leading edge of the rim seal. Experimental measurements are presented at two discrete locations on the stator platform for both bladed (solid circles) and bladeless (open triangles) configurations. The computational results are resolved for the full axial width of the vane-blade passage. Three computational datasets are included in Figure 5 for each vane position: $\Delta C_{p,a}$ in the stationary frame of reference in the presence of blades (solid lines), $\Delta C_{p,a}$ in the rotating frame with the blades (dotted lines) and $\Delta C_{p,a}$ in the stationary frame of reference without the blades (dashed lines). NB - the static pressure is common across both reference frames, however the circumferential pressure difference, $\Delta C_{p,a}$, is dependent upon whether the data is time-averaged in a rotating or stationary reference frame.

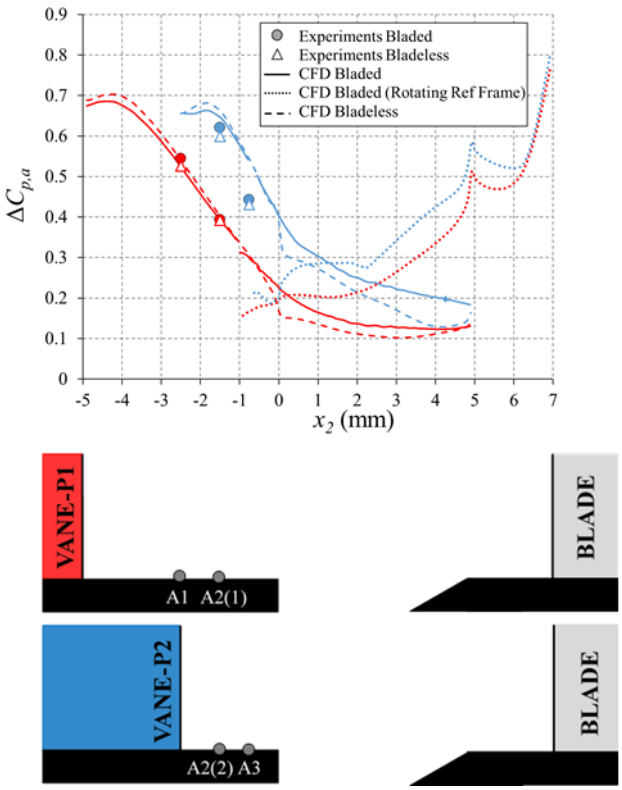

Figure 5: Axial variation of ΔC_p on the hub of the annulus plotted from the rim seal leading edge, for bladed and bladeless rotor discs ($Re_\phi = 1\times10^6$, $\Phi_0 = 0.03$)

For all configurations, $\Delta C_{p,a}$ upstream of the rim seal decreases with increasing axial distance from the vane trailing edge. Experiment and computation both show the rotor blades have little effect on $\Delta C_{p,a}$ (the *steady* static pressure variation) on the stator side of the annulus (*i.e.* $x_2 < 0$) in the stationary frame of reference. The absolute magnitudes of pressure are reduced when the blades are removed due to the reduction in downstream blockage to atmospheric discharge. However, the non-dimensional $C_{p,a}$, remains unchanged. The computational results also demonstrate the decay in $\Delta C_{p,a}$ in the rotating frame of reference with distance upstream from the leading edge of the blade. This unsteady pressure distribution, represented by the dotted lines, is equivalent to a circumferential distribution of pressure that rotates with the blades. Conventionally the rim seal is positioned equidistant between the vane trailing edge and the blade

leading edge where the variation of circumferential pressure is weakest in both the stationary and rotating frames of reference.

Figure 5 is consistent with Figure 4 and demonstrates that when plotted from the rim seal leading edge, the magnitude of $\Delta C_{p,a}$ for vane-P2 is greater than for vane-P1, both experimentally and computationally. The experiments are well predicted by the computation for the closer vane position, but not well predicted at vane position P2. The value of $\Delta C_{p,a}$ at $x_2 = 0$ is thus uncertain. This is an important point as the pressure near the rim seal has been shown to be crucial in terms of governing ingress [19] and clearly difficult to compute.

The results show the pressure distribution is virtually unaffected by the blades for $x_2 < 0$. In contrast, for $x_2 > 0$ the pressure distribution is dominated by the rotor blades, demonstrating an increased vane-blade interaction for the closer configuration (P2).

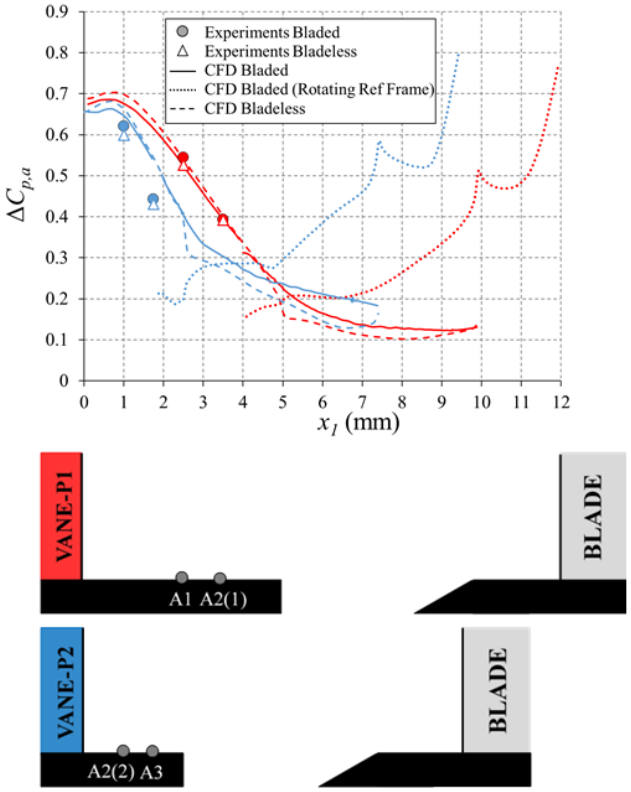

Figure 6: Axial variation of ΔC_p on the hub of the annulus plotted from the vane trailing edge, for bladed and bladeless rotor discs (Re_ϕ = 1×10^6, Φ_0 = 0.03)

An alternative method of presenting the data in Figure 5 is shown in Figure 6, where the horizontal axis is the relative distance from the vane trailing edge for both cases. This reveals that the axial decay rate in $\Delta C_{p,a}$ with distance downstream from the vane is different for the two configurations; the peak-to-trough pressure difference for vane-P2 decays more abruptly than for vane-P1. Plotted in this form the magnitude of $\Delta C_{p,a}$ for vane-P2 is unexpectedly smaller on the stator hub at an equivalent distance downstream of the stator vane. This is not due to the relative proximity of the blades, which are observed not to affect the pressure distribution. It is the location of the rim seal, and the corresponding ingress and egress through the clearance that influences the pressure variation on the stator hub platform.

There is no rim-seal influence at the shroud. Experimental and computational results are plotted along the outer casing at the shroud of the annulus in Figure 7. The horizontal axis is the relative distance from the trailing edge of the vanes. Here there is again very little influence of the blades and, in the absence of the influence of the egress/ingress through the rim seal, all four configurations collapse on a single distribution that represents the decay of the pressure from the vane.

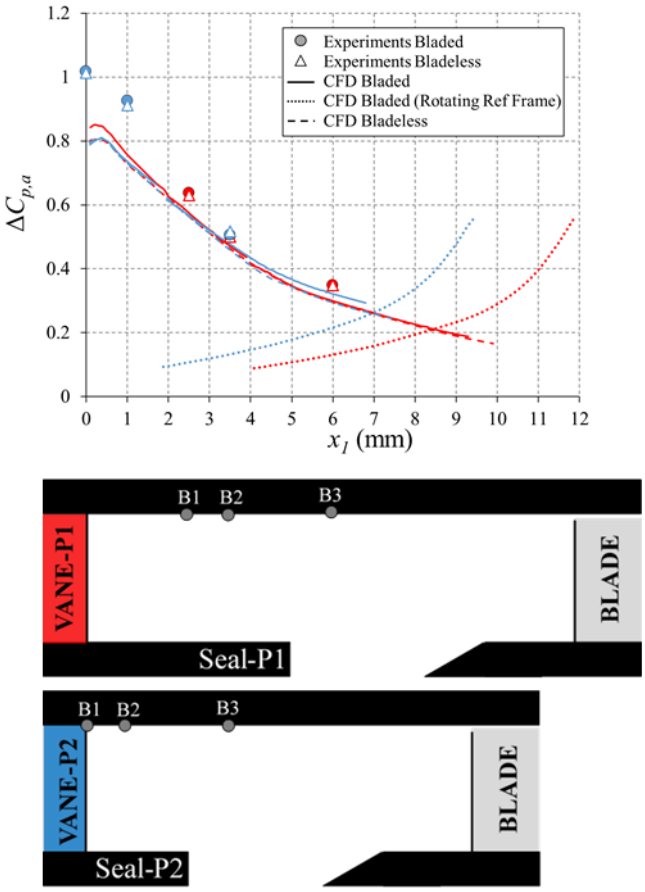

Figure 7: Axial variation of ΔC_p at the shroud of the annulus plotted from the vane trailing edge, for bladed and bladeless rotor discs ($Re_\phi = 1\times10^6$, $\Phi_0 = 0.03$)

5.2 Variation of swirl ratio with sealing flow in the wheel-space

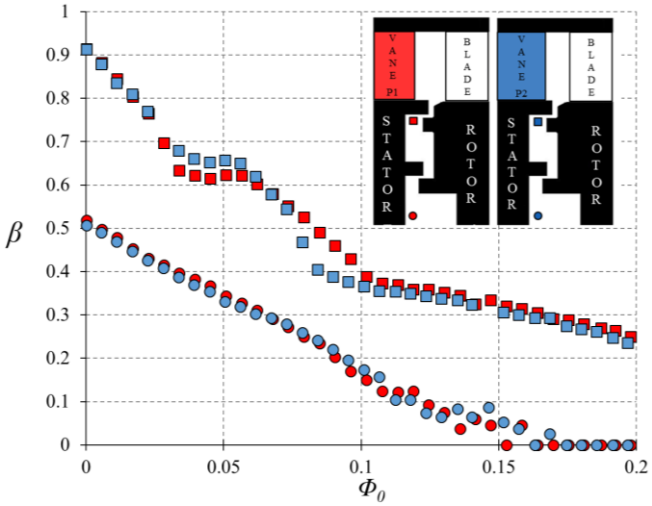

Figure 8: Measured variation of swirl ratio with non-dimensional sealing flow rate at *r/b* = 0.993 (squares) and *r/b* = 0.825 (circles), for two vane positions with rotor blades ($Re_\phi = 7.4\times10^5$)

Experimental measurements of tangential swirl were made in the wheel-space at two radial locations in the inner (*r/b* = 0.825) and outer (*r/b* = 0.993) wheel-spaces of the double radial-clearance rim seal. Figure 8 shows the variation of the swirl ratio, β, (relative to the disc speed) over a wide range of non-dimensional sealing flow rates for both vane positions in the presence of the blades. The measurement points in the wheel-space (at *z/S* = 0.25) are shown on the silhouette.

For all conditions the swirl ratio is larger in the outer wheel-space; note the swirl in the annulus is βa = 1.6 and ingress will affect the swirl here. Generally, increasing the sealing flow rate both reduces ingress and suppresses the tangential velocity, and as a result the swirl ratio reduces. Radially inboard of the inner seal there is no effect of vane position on swirl ratio, which decreases monotonically with Φ_0. In the outer wheel-space there is an inflexion in the range $0.03 < \Phi_0 < 0.08$ for both vane positions and a clear influence of the vane position. Outside of this range of purge the swirl collapse onto a curve virtually independent of vane position.

Figure 9 shows the effect of the rotor blades on the swirl in the wheel-space for vane-P2. The solid symbols are reproduced from Figure 8 whereas the open symbols represent measurements without the blades, *i.e.* a rotating disc without blades. As before, the data in the inner wheel-space collapses onto a single, monotonic curve indicating no influence of the blades penetrating through the inner seal. In the outer wheel-space there is a marked difference between the measured swirl with and without blades, but only over the range $0.03 < \Phi_0 < 0.08$; here the blades have created an inflexion in the curve, increasing β. Clearly this indicates an increase in the ingress of highly-swirling fluid from the annulus. The phenomenon is only observed over a relatively narrow range of purge; this is discussed further in Section 5.3 with reference to Fig. 12 and Section 5.4 with reference to Fig. 14. At low sealing flow rates ($\Phi_0 < 0.03$) there is insufficient egress momentum to influence the local flow conditions; at high levels ($\Phi_0 > 0.1$) the wheel-space is sufficiently sealed to prevent ingress from occurring and the effect cannot be observed.

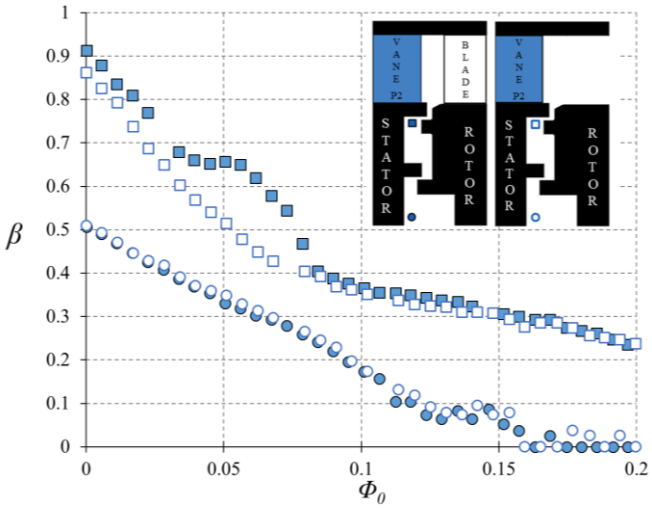

Figure 9: Measured variation of swirl ratio with non-dimensional sealing flow rate at *r/b* = 0.993 (squares) and *r/b* = 0.825 (circles), for bladed (solid symbols) and bladeless (open symbols) rotor discs ($Re_\phi = 7.4\times10^5$)

5.3 Gas-concentration measurements

Figure 10 shows the variation of effectiveness with Φ_0 for *both* vane positions in the presence of blades. Concentration was measured on the stator at r/b = 0.85 and 0.958 in the inner and outer wheel-spaces, respectively. There is an increase in ε_c with increasing Φ_0, as the wheel-space is pressurised with a reduction in ingress through the rim-seal. The ε_c - Φ_0 data collapse onto individual curves which are independent of Re_ϕ.

In the inner wheel-space, the $\varepsilon_c - \Phi_0$ curves follow a conventional monotonic form [20]. However, in the outer wheel-space there is an inflexion in the curves for $0.03 < \Phi_0 < 0.08$, a similar range of purge discussed with reference to swirl in Section 5.2 and independent of Re_ϕ. The inflexion is consistent with previously published data by Horwood *et al.* [17] for the same configuration as vane-P1. Similar inflected curves have been published by Boudet *et al.* [21], Gentilhomme *et al.* [22] and Clark *et al.* [23], though the authors do not present an explanation for the phenomenon. Here the data has been collected at a flow coefficient of C_F = 0.407 corresponding to the design point of the stage. The degree of inflexion is sensitive to the flow coefficient; measurements by Patinios *et al.* [16] for vane-P1 at C_F = 0.293 showed conventional, monotonic curves in both the inner and outer wheel-spaces.

The axial location of the vane has an influence on effectiveness in the outer wheel-space over the range $0.03 < \Phi_0 < 0.08$. Here vane-P2, which is closer to the rim seal clearance, drives higher levels of ingress into the wheel-space and therefore lower ε_c for the same Φ_0. This is consistent with the measurements and computations of pressure in the annulus presented in Figure 4 if $\Delta C_{p,a}$ is the driving mechanism governing ingress [20]. In the inner-wheel-space there is no effect of vane position and the fluid dynamics is controlled by rotationally-induced, rather than externally-induced ingress [24].

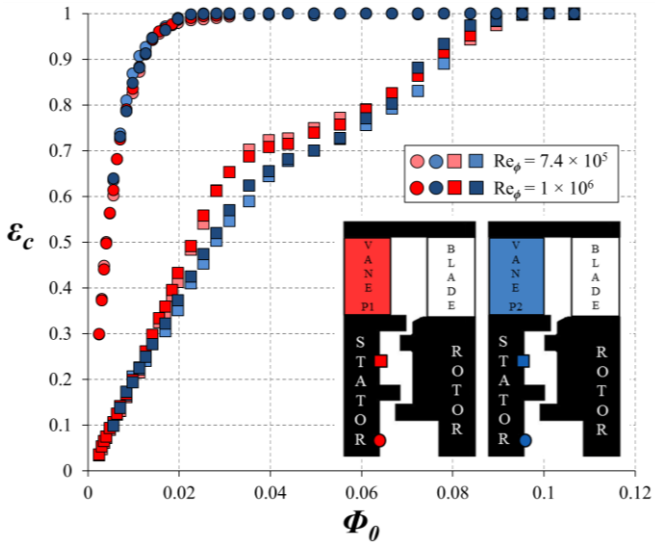

Figure 10: Variation of sealing effectiveness with non-dimensional sealing flow rate at *r/b* = 0.958 (squares) and *r/b* = 0.85 (circles), for two vane positions with rotor blades

There is clearly a connection between the inflexion in the swirl and effectiveness curves in the range $0.03 < \Phi_0 < 0.08$ in Figure 8 and Figure 10**.** Section 5.4 discusses how strong unsteady pressure fluctuations are also measured within this range of sealing flow rates.

Data in Figure 10 was collected at the stator surface. Measurements of effectiveness were also made in the core region of the outer wheel-space using the hypodermic Pitot tubes shown in Figure 3. Figure 11 shows the variation of ε_c with increasing purge at three radial locations for vane-P1. The inflexion is most pronounced nearest the periphery of the wheel-space, *i.e. r/b* = 0.993. The corresponding measurements of swirl at the same location and radius are shown in Figure 8; there is a clear correlation with both exhibiting an inflexion in the range $0.04 < \Phi_0 < 0.08$.

The measurements of effectiveness at *r/b* = 0.924 are consistent with those at the stator wall (Figure 10). The largest values of effectiveness in the core are measured at

r/b = 0.958. This pattern in radial distribution of core effectiveness is consistent with Horwood *et al.* [17], who showed that the effectiveness at r/b = 0.958 is influenced by high-concentration fluid pumped radially outwards from the rotor boundary layer.

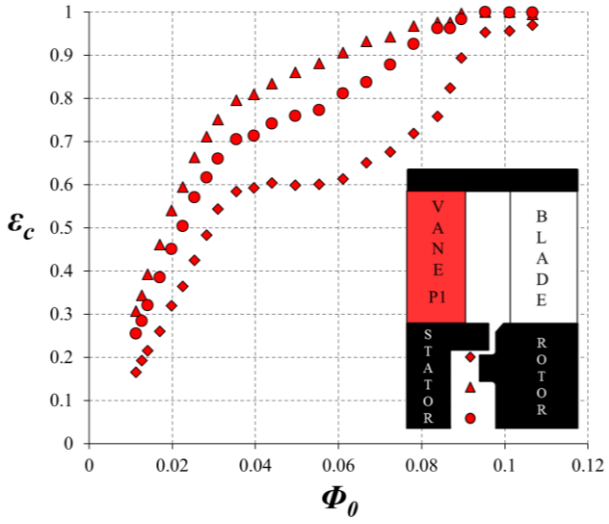

Figure 11: Effectiveness measurements in the core of the outer wheel-space at three radial locations: diamonds (r/b = 0.993), triangles (r/b = 0.958) and circles (r/b = 0.924)

Figure 12 shows the variation of effectiveness with purge for the case of a rotor disc with and without blades. Data has been collected for vane-P2, with one curve reproduced from Figure 10. There is no effect of the blades in the inner wheel-space where the effectiveness is identical for both configurations. However, in the outer wheel-space the inflexion (in the range $0.03 < \Phi_0 < 0.08$) is clearly caused by the blades; in the absence of the blades on the rotor there is a monotonic, conventional relationship between lower ε_c and Φ_0. The rotor blades clearly increase the levels of ingress over the range $0.03 < \Phi_0 < 0.08$. The data is independent of Re_ϕ and qualitatively consistent with the corresponding swirl measurements shown in Figure 9.

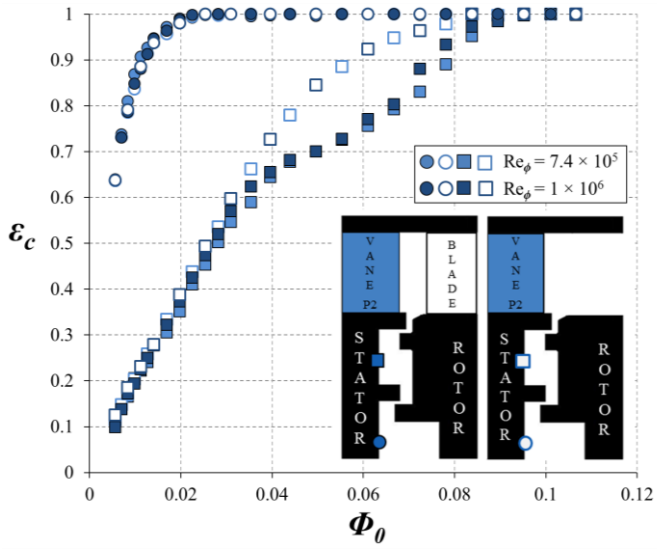

Figure 12: Variation of sealing effectiveness with non-dimensional sealing flow rate at *r/b* = 0.958 (squares) and *r/b* = 0.85 (circles), for bladed and bladeless rotor discs

Figure 13 shows the effect of vane position on ingress in the absence of blades on the rotor disc. For both the inner and outer wheel-spaces, and for both rotational speeds tested, there is no influence of vane position on the effectiveness measurements – the data collapse to a single curve independent of Re_ϕ. The results are contrary to previous findings (*e.g.* Chew *et al.* [4]), though consistent with the diffusion-model predicted by Savov and Atkins [25]. The conventional theory of externally-induced ingress predicts the ingress to be proportional to $\Delta C_{p,a}^{1/2}$ on the vane platform near the seal [20]; Figure 5 shows that the sensitivity of $\Delta C_{p,a}$ to vane position at the seal clearance is uncertain and the data poses an unresolved question as clearly the different driving pressures are not influencing the level of ingress.

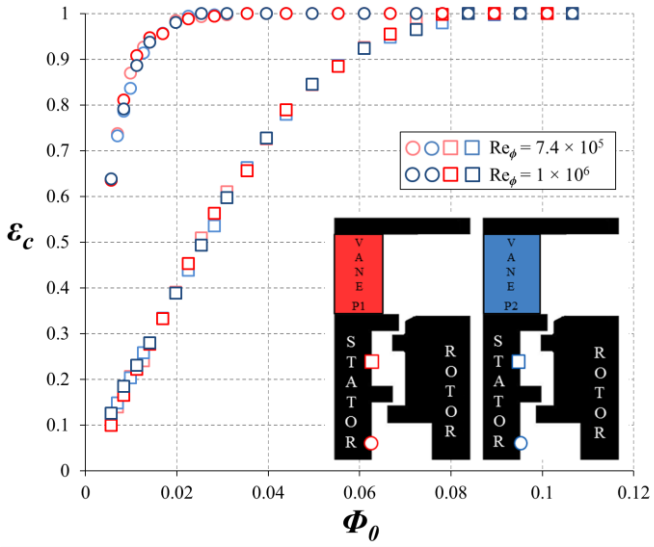

Figure 13: Variation of sealing effectiveness with non-dimensional sealing flow rate at *r/b* = 0.958 (squares) and *r/b* = 0.85 (circles), two vane positions without rotor blades

5.4 Unsteady pressure measurements

Measurements of unsteady pressure were collected at five purge flow rates, for both vane positions with and without rotor blades. These measurements reveal the presence of rotating flow structures which, as discussed in Section 2, are linked to Taylor-Couette or Kelvin-Helmholtz instabilities in and near the rim seal. The cause and effect of these phenomena are not well understood, and the objective here is to isolate the effects of the rotor blade and the relative intensity of the vane pressure distribution.

Figure 14 and Figure 15 show Fast Fourier Transformations (FFTs) for data collected with and without rotor blades (respectively) for two relative vane positions. The FFTs are based on unsteady pressure from the stator wall at *r/b* = 0.993, as shown in the silhouettes. Five sealing flows are used: Φ_0 = 0.02, 0.03, 0.05, 0.078 and 0.104 at $Re_\phi = 7.4\times10^6$. The data for vane-P1 in Figure 14 are reproduced from Horwood *et*

al. [17], who showed the results were invariant with Re_ϕ across the range listed in Table 1.

For convenience, the measurements of effectiveness in the outer wheel-space (from Section 5.3) are reproduced here to show the level of ingress; these plots are annotated to link with the FFTs. The frequencies are non-dimensionalised with f_d (the disc rotation frequency); the pressure has been non-dimensionalised as C_p - see nomenclature.

Phase analysis, using the method of described by Beard *et al.* [14], for signals from two pressure transducers offset by 8° (α) in the azimuthal direction allowed measurement of the number of structures (N) and rotational speed relative to the disc (ω/Ω). Data were collected over 10 s at 100 kHz, with the signals partitioned into individual disc revolutions. A 50 kHz low-pass filter was installed in the data acquisition system to prevent aliasing. Cross-correlated signals for each revolution determined the average lag time (Δt_α) and rotational speed ($\omega = \alpha / \Delta t_\alpha$). The number of rotating structures (N) was calculated from the normalised frequency (f / f_d) and the normalised rotational speed (ω/Ω). The data are summarised in Tables 3 (bladed rotor) and 4 (bladeless rotor).

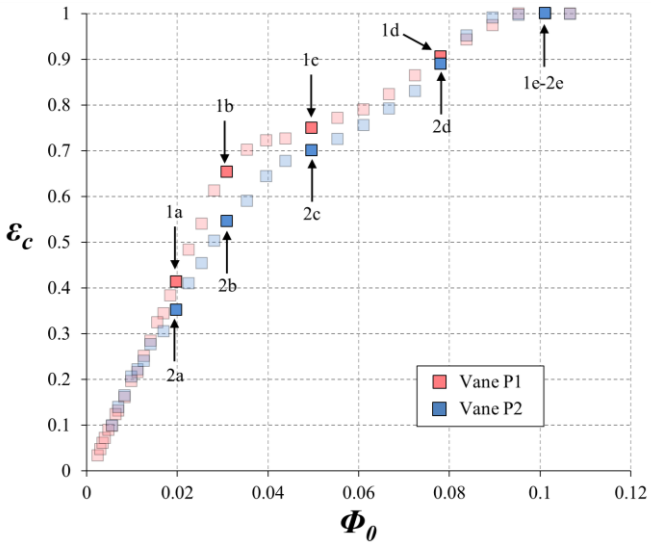

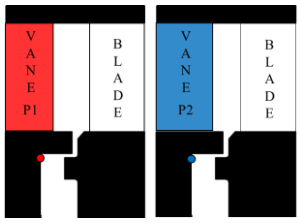
VANE P1
BLADE
VANE P2
BLADE

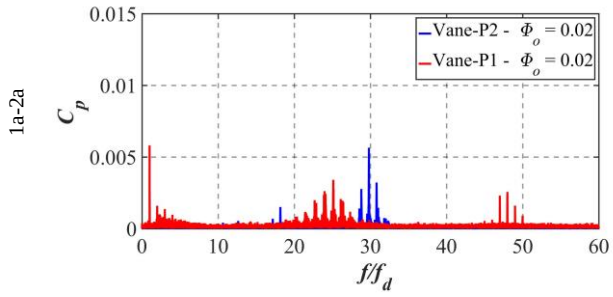
1a-2a
Vane-P2 - Φ_o = 0.02
Vane-P1 - Φ_o = 0.02
C_p
f/f_d

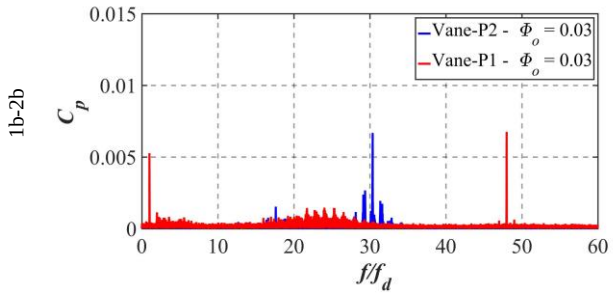
1b-2b
Vane-P2 - Φ_o = 0.03
Vane-P1 - Φ_o = 0.03
C_p
f/f_d

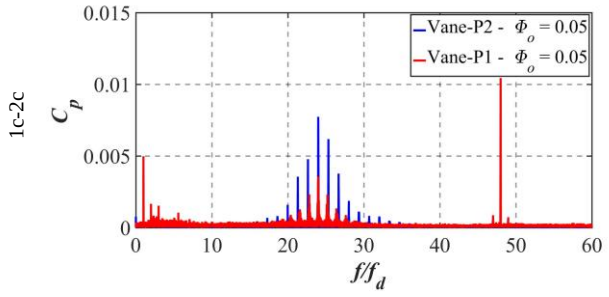
1c-2c
Vane-P2 - Φ_o = 0.05
Vane-P1 - Φ_o = 0.05
C_p
f/f_d

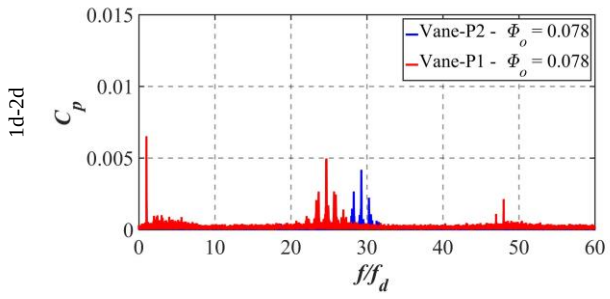
1d-2d
Vane-P2 - Φ_o = 0.078
Vane-P1 - Φ_o = 0.078
C_p
f/f_d

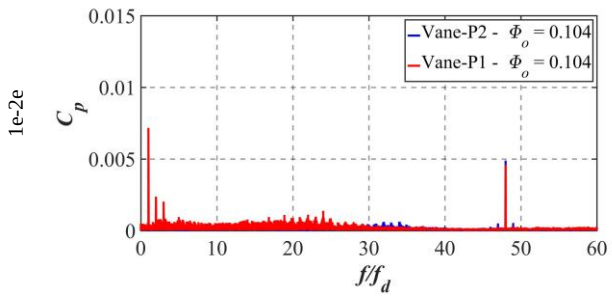

Figure 14: Fast Fourier Transforms of unsteady pressure data at *r/b* = 0.993 on the wheel-space stator wall, for two vane positions with rotor blades ($Re_\phi = 7.4\times10^5$)

Consider Figure 14, which illustrates FFTs for the two vane positions with a bladed rotor. Here $f / f_d = 48$ corresponds to the blade passing frequency (BPF) and intensity at this frequency is observed across all sealing flow rates. The experimental data appear as distinct spikes at regular intervals rather than a broad spectrum of activity, probably because the number of structures is switching between integer values. The data is sampled over 10 seconds, over which time this distinct value could switch many times; this would result in the kind of FFT shown in Fig. 14, rather than a continuous broad spectrum. Table 3 shows that the number of structures varied between $22 < N < 28$, depending weakly on the vane position and sealing flow rate. In all cases these structures rotated close to the disc speed with $0.96 < \omega/\Omega < 1.12$ (note that $\omega/\Omega > 1$ is possible given $\beta_a = 1.6$ downstream of the vanes). At $\Phi_0 = 0.02$ and $\Phi_0 = 0.03$ there are two distinct frequencies for each vane position. At $\Phi_0 = 0.05$ (for both vane positions) there is a magnification of the low frequency activity at precisely $f / fd = 24$ (*i.e.* half the blade count). The corresponding structures are calculated, within experimental uncertainty, to rotate at the disc speed, $\omega/\Omega = 1$. The development of these structures, clearly linked to the number of blades, is in the inflexion region of the $\varepsilon_c - \Phi_0$ curves**.** At $\Phi_0 = 0.078$ there are once again two distinct frequencies for each vane position and

at Φ_0 = 0.104 the wheel-space is sealed and the spectral activity for both vane positions is supressed.

	Rotor Speed (RPM)	Non-dimensional Sealing Parameter (Φ_0)	Number of Structures (N)	Rotational speed of Structures (ω/Ω)
Vane P1				
Exp	3000	0.020	26	0.96
Exp	3000	0.030	26	0.92
Exp	3000	0.050	23	1.03
Exp	3000	0.078	26	0.94
Exp	3000	0.104	N.A.	N.A.
Vane P2				
Exp	3000	0.020	26	1.10
Exp	3000	0.030	28	1.12
Exp	3000	0.050	24	0.99
Exp	3000	0.078	22	0.94
Exp	3000	0.104	N.A.	N.A.

Table 3: Comparison of large scale flow structures, for two vane positions with rotor blades

Figure 15 presents the corresponding FFTs for the two vane positions but with the bladeless rotor disc. Across all purge a single, distinct frequency is observed at f / f_d = 31 for vane-P1 and f / f_d = 28 for vane-P2. Note the switching between frequencies in the FFTs is not as pronounced as the cases with blades (Fig. 14), suggesting that the stability of these structures is influenced by the potential field of the rotating blades. Relative to experiments with the blades the magnitude of C_p is larger; this is because the FFTs with blades are composed of signals divided over several frequencies as opposed to the case without the blades, where the energy is concentrated into fewer frequencies. Data showing $34 < N < 40$ and $0.71 < \omega/\Omega < 0.89$ is summarised in Table 4. The number of structures is increased, and the rotational speed decreased, relative to the measurements with the blades. The structures for vane-P2 appear to rotate slower than vane-P1.

The measurements indicate two fundamental mechanisms driving unsteady behaviour in the rim seal region: large-scale structures that possibly arise from Taylor-Couette or Kelvin-Helmholtz instabilities, which are present even in the absence of blades; and the blade-vane interaction that acts to supress the structures or modify the frequency at which they occur.

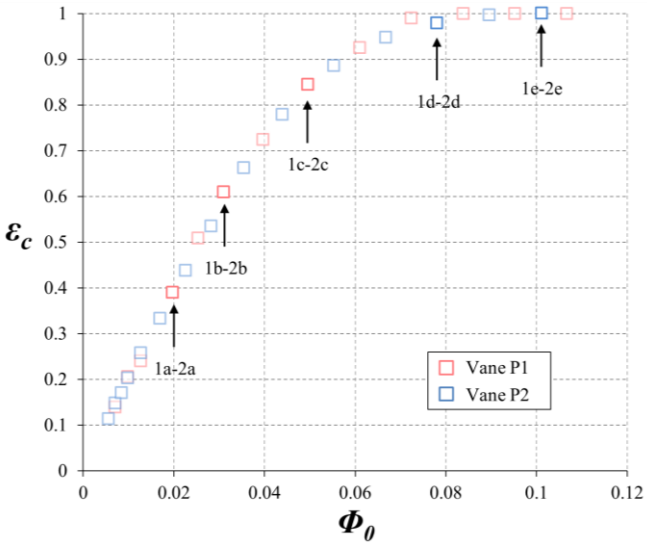
ε_c
Φ_0
1a-2a
1b-2b
1c-2c
1d-2d
1e-2e
Vane P1
Vane P2

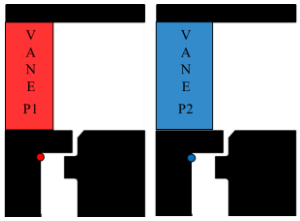
VANE P1
VANE P2

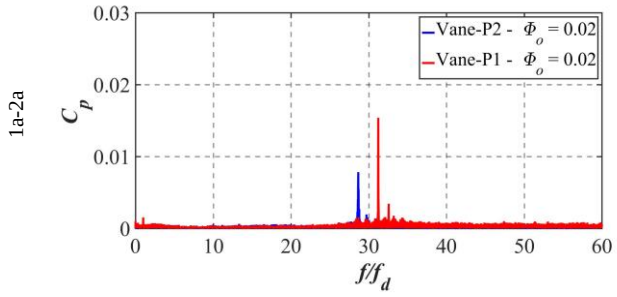
1a-2a
C_p
f/f_d
Vane-P2 - Φ_o = 0.02
Vane-P1 - Φ_o = 0.02

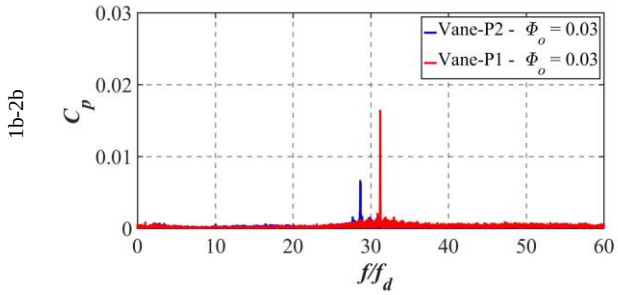
1b-2b
C_p
f/f_d
Vane-P2 - Φ_o = 0.03
Vane-P1 - Φ_o = 0.03

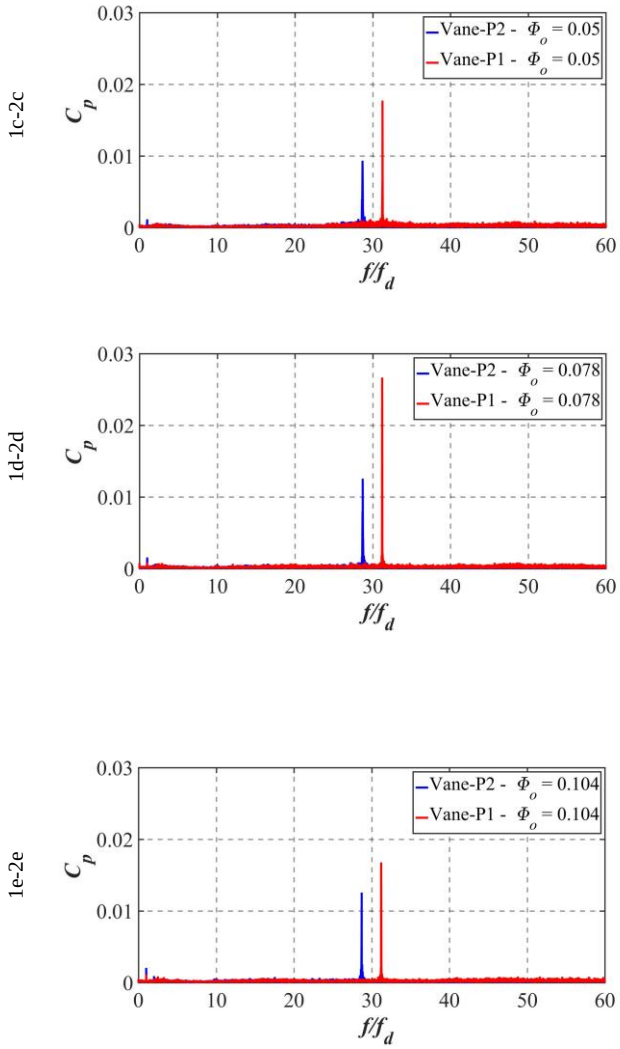

Figure 15: Fast Fourier Transforms of unsteady pressure data at *r/b* = 0.993 on the wheel-space stator wall, for two vane positions without rotor blades ($Re_\phi = 7.4\times10^5$)

	Rotor Speed (RPM)	Non-dimensional Sealing Parameter (Φ_0)	Number of Structures (N)	Rotational speed of Structures (ω/Ω)
Vane P1				
Exp	3000	0.020	34	0.89
Exp	3000	0.030	36	0.85
Exp	3000	0.050	37	0.82
Exp	3000	0.078	39	0.79
Exp	3000	0.104	39	0.79
Vane P2				
Exp	3000	0.020	37	0.74
Exp	3000	0.030	38	0.73
Exp	3000	0.050	38	0.73
Exp	3000	0.078	40	0.70
Exp	3000	0.104	39	0.71

Table 4: Comparison of large scale flow structures, for two vane positions without rotor blades

The unsteady potential pressure field from the blades does influence the large-sale structures (number N and rotational speed relative to the rotor ω/Ω), as does the level

of purge (Tables 3 and 4). At a critical range of purge ($0.03 < \Phi_0 < 0.08$) N → half the blade count and $\omega/\Omega \rightarrow 1$. Here it is speculated that the relatively-low pressure associated with these instabilities is reinforced by synchronous superposition with the unsteady pressure field from the rotating blades. This drives higher ingress (relative to the no-blade case), reducing effectiveness (Fig. 12) and increasing swirl in the wheel-space (Fig. 9). Note the annulus swirl ratio $\beta a = 1.6$.

6 CONCLUSIONS

Experimental measurements and computations have been presented for a 1.5-stage turbine rig designed to investigate ingress through rim seals. To separate effects of rotor blades and the vane-blade (or vane-rim-seal) spacing, four configurations have been investigated using two stator-vane positions and a rotor disc with and without blades.

Circumferential distributions of steady pressure across a vane pitch in the annulus have been measured and accurately reproduced computationally. The results show that the non-dimensional peak-to-trough pressure difference ($\Delta C_{p,a}$) decays with axial distance from the trailing edge of the vane. Experiment and computation both show the rotor blades have little effect on $\Delta C_{p,a}$ (the *steady* static pressure variation) on the stator side of the annulus. Far from any influence of the rim-seal, this decay on the outer shroud collapses onto a single distribution all four configurations. In contrast, at the hub of the annulus the axial rate of decay in $\Delta C_{p,a}$ with distance downstream from the vane is different for the two vane positions; this is due to the proximity of the rim seal, and the corresponding ingress and egress through the clearance that influences the pressure variation on the stator hub platform.

Measurements of swirl were made in both the inner and outer wheel-spaces of a double radial clearance rim seal for a wide range of sealing flow rates. In the inner wheel-space, no influence of the blades or vane position was observed. However, in the outer wheel-space there is a pronounced inflexion in the β - Φ_0 curve over the *critical range* $0.03 < \Phi_0 < 0.08$ with a clear influence of vane position. There is also a marked difference between the measured swirl with and without blades, but again only over the critical range of Φ_0 where the blades have created an inflexion in the curve.

Ingress in both wheel-spaces was quantified using gas concentration measurements for all four configurations. In the inner wheel-space, the ε_c – Φ_0 curves follow a conventional monotonic form. However, in the outer wheel-space there is an inflexion in the curves for $0.03 < \Phi_0 < 0.08$. The inflexion is clearly caused by the blades; in the absence of the blades on the rotor the monotonic, conventional relationship returns. The rotor blades clearly increase the levels of ingress over the range $0.03 < \Phi_0 < 0.08$. The data is independent of Re_ϕ and qualitatively consistent with the corresponding measurements of swirl.

It was also shown in the absence of blades there is no influence of vane position on ingress. This is rather surprising as conventional theory predicts ingress to be proportional to $\Delta C_{p,a}^{1/2}$ on the vane platform near the seal; however, the sensitivity of $\Delta C_{p,a}$ to vane position at the seal clearance is uncertain and the data poses an unresolved question.

Unsteady pressure measurements at the periphery of the wheel-space revealed the existence of $22 < N < 28$ large-scale pressure structures (or instabilities), the number depending weakly on the vane position and sealing flow rate. In all cases these structures rotated close to the disc speed. At $\Phi_0 = 0.05$ (for both vane positions) there was a magnification of the low-frequency activity at precisely half the blade count with

the structures calculated, within experimental uncertainty, to rotate at the disc speed. The development of these structures, clearly linked to the number of blades, is in the critical region of the $\varepsilon_c - \Phi_0$ curves. The relatively-low pressure associated with these instabilities in the seal clearance is reinforced by synchronous superposition with the unsteady pressure field from the rotating blades. This drives higher ingress (relative to the no-blade case), reducing effectiveness and increasing swirl in the wheel-space.

In the absence of blades these structures were still shown to occur but manifest themselves at greater number and at a slower rotational speed that when the blades were present.

NOMENCLATURE

A_p amplitude of unsteady pressure (Pa)

b radius of seal (m)

BPF blade passing frequency (Hz)

c concentration of tracer gas

CFD computational fluid dynamics

CFL Courant–Friedrichs–Lewy

C axial chord (m)

C_F flow coefficient ($W/\Omega b$)

Cp pressure coefficient (= $A_p / \frac{1}{2}\rho\Omega^2 b^2$)

$C_{p,a}$ pressure coefficient in annulus (= $(p_a - \bar{p}_a)/\frac{1}{2}\rho\Omega^2 b^2$)

$C_{p,s}$ static pressure coefficient (= $(p - p_{inf})/\frac{1}{2}\rho_{LE}\Omega^2 b^2$)

$C_{w,0}$ nondimensional sealing flow rate (= $\dot{m}/\mu b$)

f measured frequency (Hz)

fd frequency of disk rotations (Hz)

FFT fast Fourier transform

G_c seal-clearance ratio (= $s_{c,ax}/b$)

h height of annulus (m)

$\dot{m}$ mass flow rate (kg/s)

M Mach number

N Number of large-scale structures around disc

p static pressure (Pa)

p_T total pressure (Pa)

PCD pitch circle diameter

r radius (m)

Re_b blade Reynolds number (= $\rho W C_b/\mu$)

Re_v vane Reynolds number (= $\rho W C_v/\mu$)

Re_w axial Reynolds number in annulus based on radius (= $\rho W b/\mu$)

Re_ϕ rotational Reynolds number (= $\rho \Omega b^2/\mu$)

RPM revolutions per minute

s_c seal clearance (m)

S axial clearance between rotor and stator (m)

TRACE turbomachinery research aerodynamics computational environment

U bulk mean radial seal velocity (= $\dot{m}_0/2\pi\rho b s_c$)

URANS unsteady Reynolds-averaged Navier–Stokes

V velocity relative to blades (m/s)

V_ϕ tangential velocity (m/s)

W axial velocity in annulus (m/s)

x_1 axial distance from vane trailing edge (mm)

x_2 axial distance from rim seal leading edge (mm)

z axial coordinate (m)

α angle between unsteady pressure transducers (rad)

α_2 vane exit angle (deg)

β swirl ratio (= $V_\phi/(\Omega r)$)

β_2 relative blade inlet angle (deg)

β_3 relative blade exit angle (deg)

ΔC_p pressure coefficient in annulus (= $\Delta p_a / \frac{1}{2}\rho\Omega^2 b^2$)

Δp peak-to-trough pressure difference in annulus (= $p_{a,max} - p_{a,min}$)

Δt_α time for large scale structure to move through angle α (s)

ε effectiveness

ε_c concentration effectiveness

θ non-dimensional vane pitch

Λ degree of reaction

μ dynamic viscosity (kg/ms)

ρ density (kg/m^3)

Φ_0 non-dimensional sealing parameter (= $U/\Omega b$)

ψ blade loading coefficient

ω angular speed of large scale structures (rad/s)

Ω angular speed of rotating disc (rad/s)

Subscripts

a annulus

ax axial

b blade

LE leading edge

inf infinite

rad radial

v vane

0 sealing flow

REFERENCES

[1] Scobie, J. A., Sangan, C. M., Owen, J. M., and Lock, G. D., 2016, "Review of Ingress in Gas Turbines," ASME J. Eng. Gas Turb. Power, 138(12), p.120801.

[2] Chew, J. W., Gao, F. and Palermo, D. M., 2018, "Flow mechanisms in axial turbine rim sealing," Proc. IMechE Part C: J. Mechanical Engineering Science.

[3] Green, T. and Turner, A. B., 1994, "Ingestion into the Upstream Wheelspace of an Axial Turbine Stage," ASME J. Turbomach., 116(2), pp. 327-332.

[4] Chew, J. W., Green, T. and Turner, A. B., 1994, "Rim Sealing of Rotor-Stator Wheelspaces in the Presence of External Flow," ASME Paper 94-GT-126.

[5] Hills, N. J., Green, T., Turner, A. B. and Chew, J. W., 1997, "Aerodynamics of Turbine Rim-Seal Ingestion," ASME Paper No. 97-GT-268.

[6] Hills, N. J., Chew, J. W. and Turner, A. B., 2002, "Computational and Mathematical Modeling of Turbine Rim Seal Ingestion," ASME J. Turbomach., 124. pp. 306-315.

[7] Bohn, D. E., Johann, E. and Kruger, U., 1995, "Experimental and Numerical Investigations of Aerodynamic Aspects of Hot Gas Ingestion in Rotor-Stator Systems with Superimposed Cooling Mass Flow," ASME Paper 95-GT-143.

[8] Bohn, D. E., Rudzinski, B., Sürken, N. and Gärtner, W., 1999, "Influence of Rim Seal Geometry on Hot Gas Ingestion into the Upstream Cavity of an Axial Turbine Stage," ASME Paper 99-GT-248.

[9] Bohn, D. E., Rudzinski, B., Sürken, N. and Gärtner, W., 2000, "Experimental and Numerical Investigation of the Influence of Rotor Blades on Hot Gas Ingestion into the Upstream Cavity of an Axial Turbine Stage," ASME Paper 00-GT-284.

[10] Bohn, D. E., Decker, A., Ma, H. and Wolff, M., 2003, "Influence of Sealing Air Mass Flow on the Velocity Distribution in and Inside the Rim Seal of the Upstream Cavity of a 1.5-Stage Turbine," ASME Paper GT2003-38459.

[11] Jakoby, R., Zierer, T., Lindblad, K., Larsson, J., deVito, L., Bohn, D. E., Funcke, J., and Decker, A., 2004, "Numerical Simulation of the Unsteady Flow Field in an Axial Gas Turbine Rim Seal Configuration," ASME Paper No. GT2004-53829.

[12] Wang, C. Z., Johnson, B. V., De Jong, F., Vashist, T. K. and Dutta, R., 2008, "Comparison of Flow Characteristics in Axial-Gap Seals for Close- and Wide-Spaced Turbine Stages," ASME Paper No. GT2007-27909.

[13] Rabs, M., Benra, F.-K., Dohmen, H.J. and Schneider, O., 2009. "Investigation of flow instabilities near the rim cavity of a 1.5 stage gas turbine, "ASME Turbo Expo 2009, Paper GT2009-59965.

[14] Beard, P. F., Gao, F., Chana, K. S. and Chew, J. W., 2017, "Unsteady Flow Phenomena in Turbine Rim Seals," ASME J. Eng. Gas Turb. Power, 139(3), p. 032501.

[15] Savov, S.S., Atkins, N.R. and Uchida, S., 2017, "A Comparison of Single and Double Lip Rim Seal Geometries," ASME J. Eng. Gas Turb. Power, 139(11), p. 112601.

[16] Patinios, M., Scobie, J. A., Sangan, C. M., Owen, J. M. and Lock, G. D., 2017, "Measurements and Modelling of Ingress in a New 1.5-Stage Turbine Research Facility," ASME J. Eng. Gas Turb. Power, 139, p.012603.

[17] Horwood, J. T. M., Hualca, F. P., Scobie, J. A., Wilson, M., Sangan, C. M. and Lock, G. D., 2018, "Experimental and Computational Investigation of Flow Instabilities in Turbine Rim Seals," ASME J. Eng. Gas Turb. Power, 141(1), pp. 011028-011028-12

[18] Schadler, R., Kalfas, A. I., Abhari, R. S., Schmid, G. and Voelker, S., 2017, "Modulation and radial migration of turbine hub cavity modes by the rim seal purge flow," ASME J. Turbomach., 139(1), p. 011011.

[19] Owen, J. M., Wu, K., Scobie, J. A., Sangan, C. M., Cho, G. and Lock, G. D., 2014, "Use of Pressure Measurements to Determine Effectiveness of Turbine Rim Seals," ASME J. Eng. Gas Turb. Power, 137 (3), p.032510.

[20] Owen, J.M., 2011, "Prediction of ingestion through turbine rim seals: Part 2, Externally-induced and combined ingress," ASME J. Turbomach., 133, pp.031006.

[21] Boudet, J., Autef, V., Chew, J., Hills, N. & Gentilhomme, O., 2005, "Numerical simulation of rim seal flows in axial turbines," Aeronautical Journal, 109(1098), pp. 373-383.

[22] Gentilhomme, O., Hills, N. J., Turner, A. B. and Chew, J. W., 2003, "Measurement and Analysis of Ingestion through a Rim Seal," ASME J. Turbomach., 125. pp. 505-512.

[23] Clark, K., Barringer, M. and Thole, K., 2016, "Using a tracer gas to quantify sealing effectiveness for engine realistic rim seals," ASME Paper GT2016-58095.

[24] Owen, J. M., 2011, "Prediction of ingestion through turbine rim seals: Part 1, Rotationally-induced ingress," ASME J. Turbomach., 133, pp.031005.

[25] Savov, S. S. and Atkins, N. R., 2017, "A rim seal ingress model based on turbulent transport," ASME Paper No. GT2017-63531.

[26] Saravanamuttoo, H. I. H., Rogers, G. F. C. and Cohen, H., 2001. "Gas Turbine Theory," 5th Edition.

APPENDIX

Parameter	Analytical	CFD
Blade Loading Coefficient (ψ)	3.37	3.72
Degree of Reaction (Λ)	0.07	0.148
Vane Exit Angle (α_2)	77.5°	74.3°
Relative Blade Inlet Angle (β_2)	63.1°	56.3°
Relative Blade Exit Angle (β_3)	66.7°	76.7°
Blade Velocity Ratio (V_3/V_2)	1.15	1.58
Vane Reynolds Number (Re_v)	7.1×10^4	8.9×10^4
Blade Reynolds Number (Re_b)	8.2×10^4	1.0×10^5

Table 5: Turbine non-dimensional parameters near the hub (r = 0.1975 m), definitions and analytical values calculated from [26]

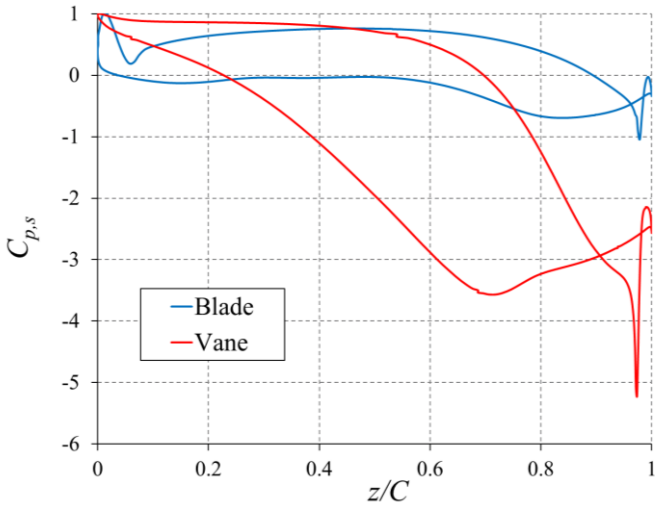

Figure 16: Computational lift distributions for vanes and blades near the hub (*r* = 0.1975 m)